

Deep-learning-based pan-phenomic data reveals the explosive evolution of avian visual disparity

Jiao Sun^{1,2}

¹Division of Ecology and Evolutionary Biology, School of Biological Science, University of Reading, Whiteknights, Reading, RG6 6EX, United Kingdom

²CAS Key Laboratory of Plant Germplasm Enhancement and Specialty Agriculture, Wuhan Botanical Garden, Chinese Academy of Sciences, Wuhan 430074, China

j.sun@pgr.reading.ac.uk

February 4, 2026

Abstract

The evolution of biological morphology is critical for understanding the diversity of the natural world, yet traditional analyses often involve subjective biases in the selection and coding of morphological traits. This study employs deep learning techniques, utilising a ResNet34 model capable of recognising over 10,000 bird species, to explore avian morphological evolution. We extract weights from the model's final fully connected (fc) layer and investigate the semantic alignment between the high-dimensional embedding space learned by the model and biological phenotypes. The results demonstrate that the high-dimensional embedding space encodes phenotypic convergence. Subsequently, we assess the morphological disparity among various taxa and evaluate the association between morphological disparity and species richness, demonstrating that species richness is the primary driver of morphospace expansion. Moreover, the disparity-through-time analysis reveal a visual “early burst” after the K-Pg extinction.

While mainly aimed at evolutionary analysis, this study also provides insights into the interpretability of Deep Neural Networks. We demonstrate that hierarchical semantic structures (biological taxonomy) emerged in the high-dimensional embedding space despite being trained on flat labels. Furthermore, through adversarial examples, we provide evidence that our model in this task can overcome texture bias and learn holistic shape representations (body plans), challenging the prevailing view that CNNs rely primarily on local textures.

Keywords bird biodiversity, deep learning, morphological evolution, interpretability, representation learning

1 Introduction

The evolution of biological morphology plays a crucial role in shaping the diverse natural world we observe today. It provides insight into the adaptation and survival of species over time,

influencing various ecological interactions and the functioning of ecosystems. Traditionally, analyses of morphological evolution have involved subjective elements, as even quantitative analyses based on morphological traits require human intervention in the selection and coding of these traits (Guillerme et al., 2020). Additionally, many features, like complex feather textures exhibited in many taxa, are hard to measure and encode in traditional morphometrics. These issues can introduce biases, affecting the accuracy and reliability of evolutionary interpretations.

To address these limitations, our research employs advanced deep learning technologies, specifically Convolutional Neural Networks (CNNs). CNNs, popularised by LeCun et al. (1989), are designed to automatically learn visual features from image data, making them exceptionally suited for visual recognition tasks. By utilising CNN image classification models, we can leverage the learned weights as indicators of morphological traits of various species, providing a more objective basis for understanding biological evolution.

In our study, we utilise CNNs as a high-throughput, high-dimensional morphometric tool capable of capturing holistic visual features, including colour, texture, and body plan. We trained a model being able to recognise over 10,000 species of birds, based on ResNet34 architecture (He et al., 2016), and calculated the cosine similarity between species using the weights extracted from the last fully connected layer (fc). This methodology enabled us to perform phenotypic disparity and macroevolutionary analysis, yielding insights into the morphological evolution of birds.

To avoid being confused with the taxonomic level “class,” the term “category” is used as an alternative to the classes of neural networks.

2 Material & Methods

2.1 Data processing

In this study, we utilised the DongNiao International Birds 10000 Dataset (DIB-10K) by Mei and Dong (2020), which comprises over 4.8 million images representing 10,922 bird species, following the IOC 10.1 taxonomy (Gill et al., 2021). This extensive dataset encompasses a wide variety of bird species, morphological variants, postures, and gestures (Mei & Dong, 2020). Despite their efforts in manual review and correction, the dataset contains numerous duplicate and erroneous images, necessitating a comprehensive data cleaning process.

For the deduplication, we employed the pHash method to detect near-duplicate images by comparing these hashes (Farid, 2021). Duplicates spanning multiple categories are completely removed, and for intracategory duplicates, only one copy is retained in its category.

To address erroneous images with non-avian subjects, we utilised the pretrained Faster Region-based Convolutional Neural Network (Faster R-CNN, Ren et al., 2017) in the torchvision library (Ansel et al., 2024). For images where no birds were detected, we implemented a two-tiered approach: images from high-volume categories (≥ 200 images) were automatically deleted, while those from low-volume categories (< 200 images) were moved to a separate directory for manual inspection. After a manual thorough review, valid images were reintegrated into the dataset.

2.2 Model training

The task of recognising over 10,000 bird species is a fine-grained visual categorisation (FGVC) problem, where the goal is to identify minor differences between highly similar categories. To tackle this challenge, we adopted the MetaFGNet model proposed by Zhang et al. (2018), which is specifically designed for FGVC tasks. We utilised their pretrained weights “LBird-31_checkpoint” as the foundation for transfer learning on the processed DIB-10K dataset. In the training process, all species are regarded as equal categories, without any *a priori* taxonomic knowledge being introduced.

For the training process, we employed a server equipped with an RTX 4090D GPU, 90GB of memory, and a 15-core Intel® Xeon® Platinum 8474C processor from the [AutoDL platform](#). This high-performance setup allowed for efficient processing and model training. The training procedure was conducted for 32 epochs.

We reassigned the orders and families of all species (categories) to align with the IOC 15.1 (Gill et al., 2025). The weights are extracted from the final fully connected layer (fc) of the ResNet34 model. Weights of each species were regarded as a 512-dimensional vector representing the morphological traits. They are reduced to the lowest boundary that can explain 80% of all variances for subsequent analyses. Gradient-weighted Class Activation Mapping (Grad-CAM, Selvaraju et al., 2020) is employed to visualise the model’s attention on images. We furtherly utilise aenerative adversarial examples with a semantic conflict between the object’s body plan and feather texture, to evaluate the priority between texture versus shape.

2.3 Similarity clustering

Species similarity was quantified using cosine similarity, implemented via dot product calculation of L_2 -normalised vectors in PyTorch (Ansel et al., 2024). Next, we conducted agglomerative hierarchical clustering using the average linkage method to merge clusters. This was executed with the hierarchical clustering functionalities implemented in the SciPy library (Gommers et al., 2025). The hierarchical structure of the clusters was output in Newick format, a widely used format in computational biology for tree structures. Finally, we utilised ETE3 to export the clustering dendrogram in SVG format (Huerta-Cepas et al., 2016).

To analysing the clustering result, we applied a recursive top-down analysis to the tree, evaluating each internal node for taxonomic “purity.” For a given node, we defined taxonomic purity as the proportion of the majority taxon. A node with a taxonomic purity of more than 85% was considered taxonomically consistent. For taxonomically consistent nodes, all of their child nodes were excluded from further checks. For such nodes, we further examined all species to identify and annotate taxonomical outliers, which belong to taxa that different from the majority taxon of this branch. Finally, we conducted manual review to confirm whether outliers had biological similarity with the majority taxa of their branches and what kinds of similarity do they have. The above pipeline was carried out in both order-level and family-level.

2.4 Disparity analysis

Before proceeding with this analysis, we removed 249 species whose weight vectors were identified as lacking biological significance during the manual review process. The specific reasons

are detailed in the discussion section.

Spherical vector variance of species is utilised to assess the morphological disparity among taxa. The Spearman's rank correlation was employed to examine the relationship between diversity (species richness) and morphological disparity (spherical variance), where taxa with $N < 2$ were excluded. The Akaike information criterion (AIC) was employed to assess and compare four models:

1. Power law: $f(x) = 1 - x^b$, the coefficient of x^b is fixed as 1 to satisfy the boundary condition $f(1) = 0$, reflecting the theoretical expectation;
2. Stretched exponential model: $f(x) = 1 - \exp(-\lambda \cdot (x - 1)^\beta)$;
3. Hill equation: $f(x) = \frac{(x-1)^n}{k+(x-1)^n}$;
4. Logarithmic rational model: $f(x) = \frac{\ln(x)}{k+\ln(x)}$.

All analyses were conducted at both order and family levels. Subsequently, the residuals of the disparity of every taxon are calculated, five taxa with the highest and five with the lowest residuals are listed.

Additionally, we explore the relationship between taxa size and mean pairwise angle, taxa size and pairwise angle variance, as well as mean pairwise angle and pairwise angle variance at both order and family levels. For size vs variance analysis, taxa with $N < 3$ were excluded to avoid mathematical artefacts (variance = 0 for $N = 1$ or 2). For the other two analysis (mean angle), taxa with $N < 2$ were excluded.

2.5 Disparity through time

In classical phylogenetic independent contrast (PIC) proposed by Felsenstein (1985), The evolution of phenotypic traits follows a Brownian motion model in Euclidean space, in which the trait of each descendant is derived from the trait of the ancestral species through a random walk in Euclidean space. The time of this walk is proportional to the divergence time, which is the branch length of the evolutionary tree.

As demonstrated by Wang et al. (2017), in the last fully connected layer of CNNs, the semantic information is primarily encoded in the angular direction, which is equivalent to L_2 normalised vectors. Therefore, we assume that the feature vectors randomly walk on a unit hypersphere. We implemented the algorithm for Spherical Ancestral State Reconstruction by modeling phenotypic evolution as Riemannian Brownian Motion on the hypersphere of the deep feature space in Python.

In a post-order traversal of the phylogenetic tree, for a selected pair of sister nodes (sister groups), let $\mathbf{v}_a, \mathbf{v}_b$ be the state vectors of them on a unit hypersphere, and l_a, l_b be their branch lengths (for leaf nodes) or the equivalent branch lengths (for internal nodes) on a timetree. Let \mathbf{v}_p be the feature vector of their parent node (most recent common ancestor), it must be on the two-dimensional Euclidean plane spanned by \mathbf{v}_a and \mathbf{v}_b . The ancestral state and the contrast is computed via the following steps fig. 1:

1. We firstly calculate their geodesic distance, which is equivalent to their included angle for L_2 normalised vectors:

$$\theta = \arccos(\mathbf{v}_a \cdot \mathbf{v}_b) \quad (1)$$

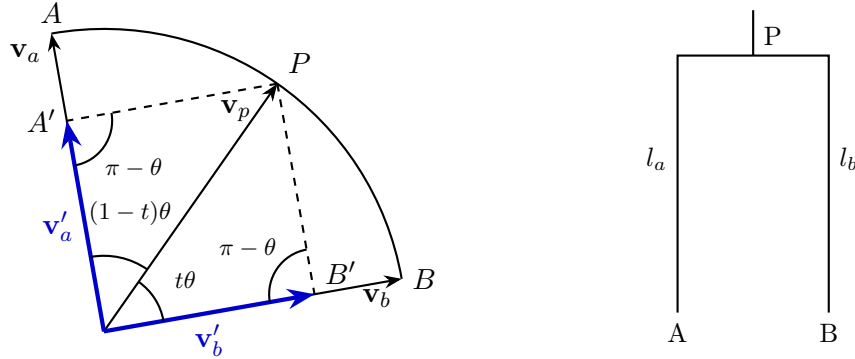


Figure 1: Geometric diagram of the ancestor state reconstruction algorithm.

2. The parent state \mathbf{v}_p is inferred by interpolating along the geodesic arc:

$$\mathbf{v}_p = \frac{\sin((1-t)\theta)}{\sin \theta} \mathbf{v}_a + \frac{\sin(t\theta)}{\sin \theta} \mathbf{v}_b \quad (2)$$

where $t = l_b/(l_a + l_b)$.

3. To adjust for the curvature of the state space, the contrast variance is scaled by the ratio of the squared arc length to the squared chord length:

$$\text{Contrast}^2 = \underbrace{\frac{(\mathbf{v}_a - \mathbf{v}_b)^\circ 2}{l_a + l_b}}_{\text{Euclidean Variance}} \times \underbrace{\frac{\theta^2}{\|\mathbf{v}_a - \mathbf{v}_b\|^2}}_{\text{Correction Factor}} \quad (3)$$

where \circ means Hadamard power (element-wise power).

4. When the traversal is completed, the estimated evolutionary rate of the whole tree is:

$$\hat{\sigma}^2 = \frac{\sum \text{Contrast}^2}{N - 1} \quad (4)$$

where N is the numbers of leaf nodes (species).

Once the whole ASR process is finished, the spherical variance for every time slice (1 ma) is calculated on the whole timetree, which represents the phenotypic disparity of all birds at the specific time. Then, we conduct 100 times of null simulations based on Brownian motion model in preorder traversals. For every internal node, the feature vectors of its children are calculated according to the following algorithm (fig. 2):

1. Create a Gaussian noise \mathbf{v}_x in the Euclidean space following this multivariate normal distribution:

$$\mathbf{v}_x \sim \mathcal{N}(\mathbf{0}, \hat{\sigma}^2 t \mathbf{I}_D) \quad (5)$$

where t is the evolution time (branch length) of the child node.

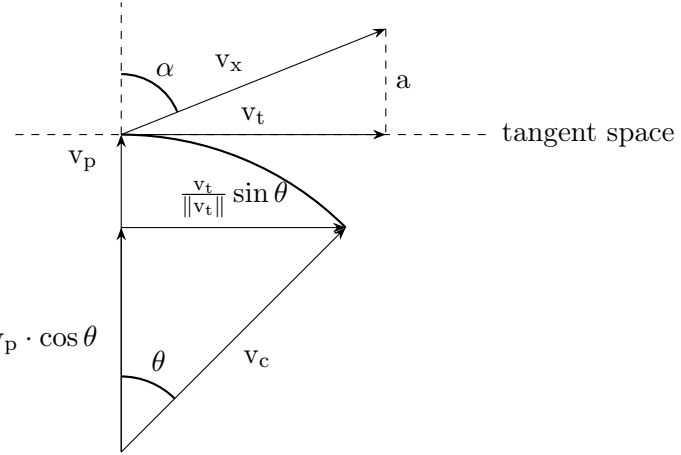


Figure 2: Geometric diagram of the brownian motion simulation algorithm.

2. Project \mathbf{v}_x onto the tangent space of the hypersphere:

$$a = \mathbf{v}_p \cdot \mathbf{v}_x \quad (6)$$

$$\mathbf{v}_t = \mathbf{v}_x - a\mathbf{v}_p \quad (7)$$

3. Move on the hypersphere following a great circle, the direction and geodesic distance is same as the direction and the norm of \mathbf{v}_t :

$$\theta = \|\mathbf{v}_t\| \quad (8)$$

$$\mathbf{v}_c = \cos \theta \mathbf{v}_p + \frac{\sin \theta}{\|\mathbf{v}_t\|} \mathbf{v}_t \quad (9)$$

and \mathbf{v}_c is the simulational feature vector of the child species.

When the whole traversal is finished, the ASR is conducted based on the simulational feature vectors of all modern species (leaf nodes) following the aforementioned algorithm, as well as the spherical variance for every time slice. Finally, the empirical disparity through time result and the mean disparity through time of all 100 times of null simulations are visualised and compared. The whole disparity-through-time analysis is conducted on the trees by Stiller et al. (2024).

3 Results

3.1 Model training and its basic characteristics

The model achieved 90.8% accuracy on the training set and 87.6% accuracy on the validation set. Grad-CAM reveals that the network's attention is focused on birds, effectively ignoring complex backgrounds and occlusions. The attention maps cover the entire bird, indicating that the extracted phenotypic vectors can be regarded as representations of the shape, plumage, and colour of species (fig. 3).

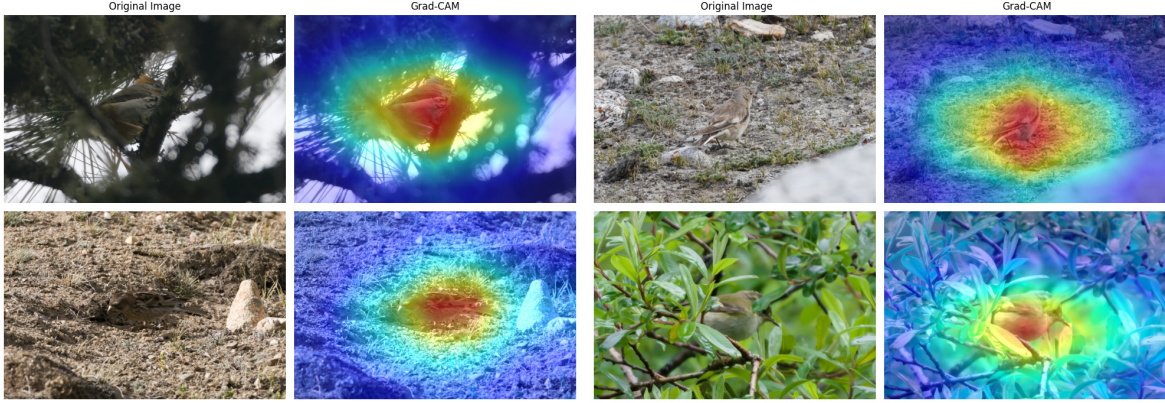


Figure 3: Grad-CAM reveals that the network’s attention is consistently focused on birds, ignoring backgrounds and occlusions.

The global mean pairwise angle across all birds is approximately 1.57066 radians ($\approx \frac{\pi}{2}$), with a low variance (≈ 0.00968). In contrast, the intra-taxa distributions (families and orders) exhibit significantly lower mean angles (≈ 1.2) but higher variances (peaking at $\approx 0.02=0.03$) (fig. 4).

A strong positive correlation exists between taxa size and mean pairwise angle (Orders: $\rho = 0.91$; Families: $\rho = 0.75$). Mean pairwise angle shows weak correlation with angle variance (Orders: $\rho = 0.33$; Families: $\rho = 0.47$). Conversely, taxa size shows weak or no correlation with angle variance (Orders: $\rho = 0.24, p > 0.05$; Families: $\rho = 0.34$).

3.2 Similarity clustering

The clustering process results in a comprehensive hierarchical clustering output. The agglomerative clustering technique applied to the cosine similarity measures of the weight vectors yielded a dendrogram that illustrates the relationships between the different avian species based on their morphological features learned by the ResNet34 model.

In the taxonomic consistence analysis, we identified a total of 391 branches with high taxonomic consistency at the family level and 94 branches at the order level. Additionally, we found 474 family-level outlier species and 533 order-level outlier species (fig. 5).

3.3 Disparity analysis

Regarding the relationship between order-level disparity and diversity, the Spearman’s coefficient is at 0.966, with a p-value of 1.45×10^{-24} . For families, the Spearman’s coefficient was 0.908, with a p-value of 3.56×10^{-83} .

The stretched exponential model receives the lowest AIC (-251.33) at the order level, followed by the Hill equation (-250.02), without significant difference ($\Delta AIC = 1.31$). The models are respectively $f(x) = 1 - \exp(-0.1420(x-1)^{0.3081})$ and $f(x) = \frac{(x-1)^{0.3973}}{7.4957+(x-1)^{0.3973}}$. Orders with the highest disparity residuals are Falconiformes, Cuculiformes, Pelecaniformes, Mesitornithiformes (highest first), and Piciformes. Caprimulgiformes, Procellariiformes, Apterygi-

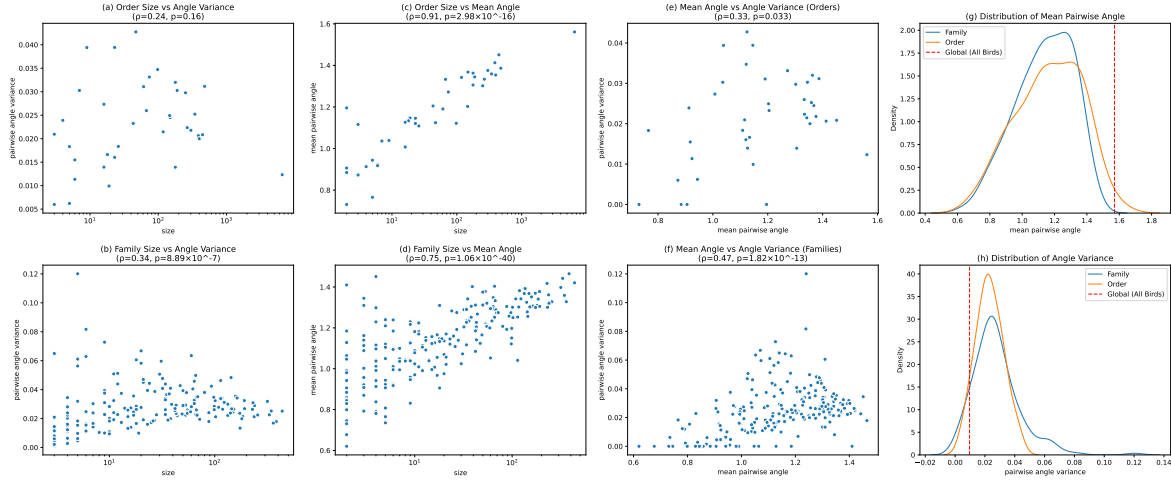


Figure 4: (a-f) The relationship between taxa size and mean pairwise angle, taxa size and pairwise angle variance, as well as mean pairwise angle and pairwise angle variance at both order and family levels. Spearman’s rank coefficients (ρ) and p-values are listed for each figure; (g-h) the distribution of mean pairwise angle and pairwise angle variance of families and orders, the mean values of all birds are marked as the red dash line.

formes, Struthioniformes, and Psittaciformes (lowest first, the same applies below) show the least disparity residuals (fig. 6a).

For families, the power law receives the lowest AIC (-1201.08), followed by the Hill equation (-1199.76), without significant difference ($\Delta AIC = 1.32$). The models are respectively $f(x) = 1 - x^{-0.1429}$ and $f(x) = \frac{(x-1)^{0.3723}}{6.0303 + (x-1)^{0.3723}}$. Mitrospingidae, Vangidae, Oreoicidae, Ptiliognathidae, and Modularicidae show the highest disparity residuals, and Apodidae, Rhinocryptidae, Caprimulgidae, Hydrobatidae, and Procellariidae show the lowest (fig. 6b).

3.4 Disparity through time

The disparity-through-time (DTT) analysis reveals an early-burst pattern for the evolution of avian visual morphospace. As shown in fig. 7, the empirical data of relative disparity deviates extremely from the expectation of Brownian Motion null simulation.

Following the K-Pg mass extinction (66 Mya), the empirical disparity immediately increases at an intense rate. This curve is consistently higher than the mean null expectation throughout the Paleogene and Neogene, resulting in a positive Morphological Disparity Index (MDI).

Crucially, the empirical curve achieves approximately 50% of the modern disparity shortly after the K-Pg mass extinction, followed by a relative deceleration towards the present. Conversely, the BM model requires significantly more time to reach the same disparity.

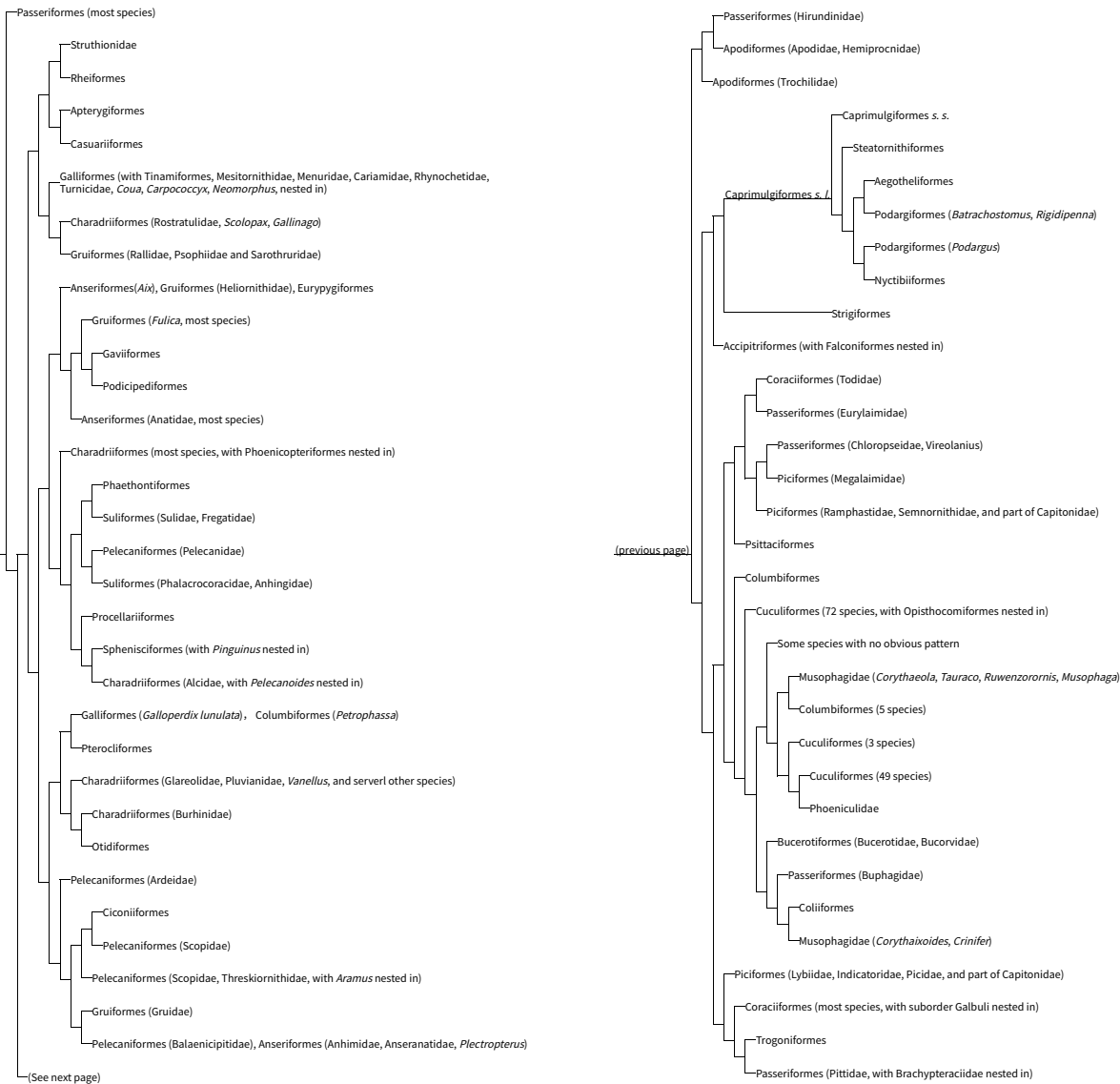


Figure 5: The unrooted clustering result with high-purity branches collapsed.

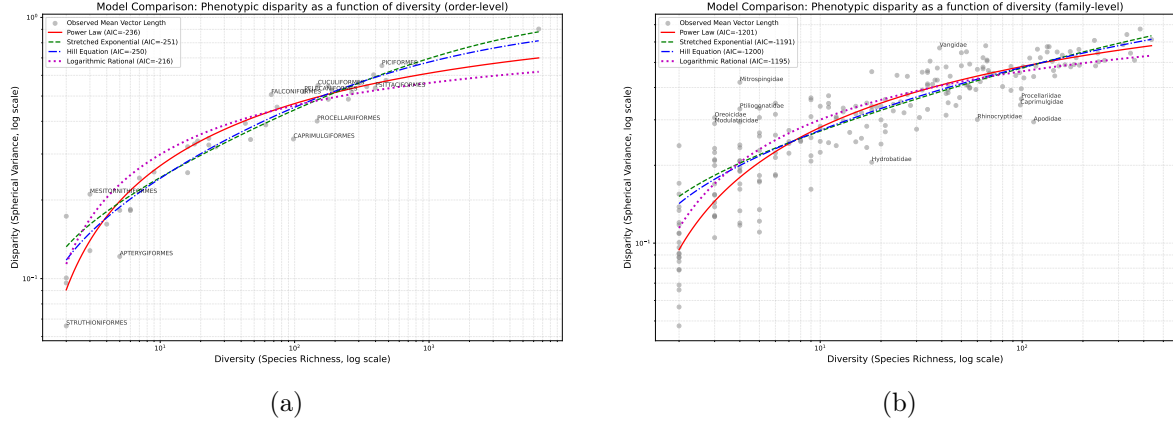


Figure 6: Comparison of models of the phenotypic disparity of taxa (orders or families) as a function of diversity. Showing scatter plot of all taxa, graphs of four models, names of the five taxa with the highest and the five with the lowest phenotypic disparity.

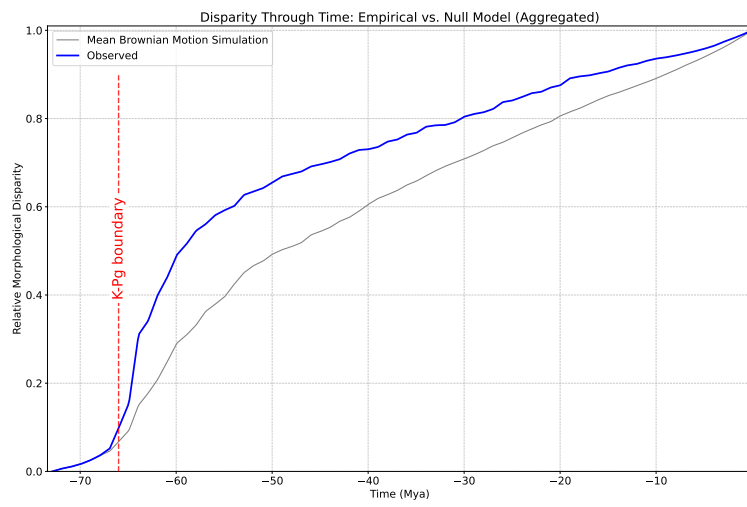


Figure 7: Relative disparity-through-time (DTT) plot for avian visual morphospace. The solid blue line represents the empirical disparity, while the solid grey line indicates the mean expectation under a multivariate Brownian Motion (BM) null model. Both empirical and simulational data are normalised relative to the disparity of the extant time (0 Mya). The K-Pg boundary (66 Mya) is marked as the red dash line.

4 Discussion

4.1 Geometry of the morphospace

The geometric analysis of the feature space reveals a distinctive interplay between high-dimensional properties and evolutionary constraints. The mean pairwise angle of $\frac{\pi}{2}$ aligns with the property of high-dimensional spaces where random vectors tend to be orthogonal and equidistant (fig. 4). Intra-taxa pairwise angles, although varied across taxa, are smaller than the global mean value. Since it is trained solely on species classification (flat labels), a hierarchical taxonomic structure (Order/Family) automatically emerges in the high-dimensional feature space. This demonstrates that feature vectors are semantically clustered, a biological taxa occupying specific sub-manifolds and therefore exhibiting smaller mean pairwise angle. This indicates that biological relationships are strongly encoded in morphological features that models have to learn this structure when searching for the optimal classification structure.

In the raw result of the clustering, many extinct species clustered together, possibly due to their representation via skeletal images, artistic reconstructions, or other non-biological patterns, being fundamentally different from extant species. Furthermore, some of the recently described species or newly separated cryptic species grouped together, being indistinguishable, which might reflect insufficient image data, leading to underfitting of the model. All extinct species and some of the newly described or newly split species, totally 249 species, were removed in subsequent analyses.

Although the clustering result is not perfectly align with current taxonomy, these inconsistencies exhibits some historically noted morphological similarity.

In the Palaeognathae, four orders (Struthioniformes, Rheiformes, Casuariiformes, Apterygiformes) of flightless birds form a distinct cluster, being driven by their unique body plans. In contrast, Tinamiformes represents a notable exception, which is deeply within the Galliformes. This topological incongruence highlights their convergent evolution. Tinamiformes and many Galliformes have evolved highly convergently, exhibiting compact body shapes for ground-dwelling lifestyles, and occupy similar niches (Glenny, 1946). The model correctly identifies this ecological and morphological similarity (fig. 5).

Furthermore, the inclusion of other visually quail-like terrestrial taxa like Turnicidae (Buttonquails) (Rotthowe & Starck, 1998), Menuridae (Winkler et al., 2020b), Neomorphus (Haffer, 1977) within the Galliformes cluster further validates that our model’s feature space captures morphological and ecological convergent adaptation and visual similarity. In the eyes of CNNs, as long as you scratch for food and run around on the ground like a landfowl, then you are a “landfowl” (fig. 5).

The clustering of Caprimulgiformes *sensu lato*, Strigiformes, Accipitriformes, and Falconiformes forms a visually similar group (fig. 5), with two layers of convergent evolution: Strigiformes and Caprimulgiformes *s. l.* share large eyes and cryptic plumage patterns for their nocturnal habits; and Strigiformes, Accipitriformes, and Falconiformes share the raptorial facial characteristics like forward-facing eyes and hooked beaks (Fidler et al., 2004; Wu et al., 2021).

Other notable similarity exhibited in the clustering result includes Hirundinidae and Apodi (Apodidae and Hemiprocnidae) (Norberg, 1986), Sphenisciformes (Penguins), Alcidae and Procellariiformes (Cody, 1973), as well as Phaethontiformes, Suliformes, and Pelecanidae (Hedges & Sibley, 1994) . . . (fig. 5) It’s demonstrated that the feature vectors’ distribution

in morphological space is not arbitrary, but is constrained by objective phenotypic similarity. Considering that we did not introduce *a priori* taxonomic knowledge in the training process, it actually reinvented the classical taxonomy from Linnaeus to Audubon. The model’s taxonomy is based on phenotype, yet with higher throughput of data than classical taxonomy and morphometrics. This naturally creates a gap compared to molecular phylogenetic trees. The gap represents the disconnection between visual disparity and genetic distance.

4.2 Shape vs Texture

Recent critiques in computer vision suggest that CNNs are biased towards textural features rather than the whole shapes (Geirhos et al., 2019). However, the aforementioned discussion on the geometry of our model’s morphospace implies that our model mainly focuses on the body plan rather than textures, challenge this assumption in the context of fine-grained visual classification.

For instance, in the previously discussed phenotypic resemblances, Hirundinidae and Apodidae shares similar aerodynamic characteristics for the aerial insectivorous niche. The instance of Sphenisciformes, Alcidae, and Procellariiformes constitutes a more convincing argument. Penguins (Sphenisciformes) have highly specialised feathers, being extremely dense, thick, and visually scale-like (Williams et al., 2015). Although Williams et al. (2015) demonstrates that emperor penguins (*Aptenodytes forsteri*) do have filoplumes and plumules, they are highly likely to be invisible in most images. While auks (Alcidae), albatrosses, petrels and shearwaters (Procellariiformes) have typical and normal feathers. If a model is textures biased, the three orders cannot be placed adjacently in the morphospace.

This hypothesis is further supported by our Grad-CAM analysis (fig. 3), which shows activation maps covering the entire avian body rather than specific patches. This indicates that our model are capable of capturing holistic representations, mirroring the concept of ‘body plan’ in biology.

To test this hypothesis, we used Google Nano Banana (gemini-2.5-flash-image) to generate a penguin with typical feathers. Our model successfully classified this adversarial example as an Adélie penguin (*Pygoscelis adeliae*) with the highest confidence, and the top-3 predictions are all penguins (fig. 8). This finding suggests that the feature vectors captured by our deep learning framework is biologically grounded. The model has learned knowledge on the macrostructure (body plan) rather than merely textures, thereby reinforcing the biological credibility of the subsequent morphological disparity analysis.

4.3 Macroevolution of birds

The Spearman’s rank correlation demonstrates that species richness is the primary driver of morphospace expansion. The strong positive correlation between taxon size and hyperspherical variance (Orders: $\rho = 0.966$; Families: $\rho = 0.908$) confirms that as clades diversify, they tend to colonise a larger volume of the visual feature space. This pattern is consistent with the “niche filling” model (Simpson, 1944), where speciation events are often associated with the exploration of novel regions in the phenotypic landscape to minimise competition. However, this expansion exhibits diminishing returns (fig. 6), suggesting that the marginal gain in disparity decreases as taxa become extremely large.

In contrast, structural heterogeneity appears to be constrained that is largely independent



Figure 8: The adversarial example of a chicken-plumaged penguin generated with Google Nano Banana. It was cropped to the bird using Faster R-CNN, and then fed into the model. Results are: Adélie penguin (*Pygoscelis adeliae*) 36.51%, yellow-eyed penguin (*Megadyptes antipodes*) 11.67%, and little penguin (*Eudyptula minor*) 8.58%.

of diversity. At the order level, angle variance is statistically independent of clade size ($\rho = 0.24, p > 0.05$), and at the family level, the correlation is weak ($\rho = 0.34$). This implies that even as a clade radiates swiftly, its internal geometric uniformity does not change chaotically but remains confined within a stable range.

In the top-5 families with high disparity residuals, four of them are newly recognised based on molecular phylogeny, indicating that they exhibit greater heterogeneity than long-established taxa, which is why they remained unrecognised by zoologists for a long time.

Vangidae is a textbook example of the radiation evolution. Although there aren't many species (39), they have evolved a variety of forms on Madagascar, ranging from shrike-like and flycatcher-like to finch-like species (Jónsson et al., 2012; Reddy et al., 2012). The model captures this extreme morphological difference, producing a very high positive residual.

Similarly, Cotingidae is given the seventh-highest disparity residual among families. Their differences in appearance are extremely eye-catching, ranging from the brightly coloured cocks-of-the-rock (*Rupicola*) to the relatively dull-coloured pihas (*Lipaugus* and *Snowornis*), with huge differences (Winkler et al., 2020a).

The disparity-through-time (DTT) analysis (fig. 7) exhibits a convex shape, suggesting that morphological disparity increased rapidly after the K-Pg mass extinction. This furtherly supports Simpson's (1944) adaptive radiation and the niche filling hypothesis. After mass extinctions vacated ecological niches, birds rapidly evolved extreme morphological diversity to occupy these positions. The surviving avian lineages rapidly radiated to fill the ecological niches, establishing the major disparate body plans (visual morphotypes) within a short geological window. The positive Morphological Disparity Index (MDI), evidenced in fig. 7, reinforces that the initial partitioning of the visual morphospace was significantly faster than neutral drift expectations.

4.4 Inspirations for further macroevolution studies

Compared to traditional morphometric methods, our novel technique exhibits both advantages and disadvantages. The most significant benefit is the high-throughput, it provides higher dimensional data and may capture features hard to quantify in traditional geometric morphometrics. Additionally, this method is independent of specific anatomy of organisms, therefore being capable of studying the macroevolution of phenotypically distinct organisms, for instance, comparing the phenotypic disparity of animals, fungi, and plants.

In contrast, the difficulty in aligning extinct species with extant birds highlights its limitations. This method also has difficulties in measuring inner structure of organisms. Moreover, despite our previous discussion on the interpretability of models, this is still a major weakness of this novel method, especially compared to geometric methods. This also restricts its applicability in comparative studies on the difference (mosaic evolution) between different body parts (e.g., beak vs. claw) or different geometrics (e.g., full length vs. weight).

Therefore, Our methodology is not a suppression or negation of the traditional methods. Rather, it serves as an important supplement to the traditional one. They can be incorporated and synthesised to provide more insights in the macroevolution of life.

5 Conclusion

This study demonstrates that deep learning models can function as high-throughput instruments for quantifying morphological disparity. By extracting weights from a ResNet34 model trained on over 10,000 bird species, we established a high-dimensional morphospace that aligns with biological taxonomy and encodes evolutionary convergence, despite the model being trained on flat labels without *a priori* taxonomic knowledge.

Our investigation into the interpretability of these networks challenges the prevailing view that CNNs rely primarily on local textures. Through the use of adversarial examples and Grad-CAM analysis, we provide evidence that the model overcomes texture bias to learn holistic shape representations, effectively capturing the “body plan”.

In the context of macroevolution, our analysis reveals that species richness acts as the primary driver of morphospace expansion, a pattern consistent with the “niche filling” hypothesis. Furthermore, the disparity-through-time analysis uncovers a visual “early burst” following the K-Pg extinction, wherein avian lineages rapidly colonised approximately 50% of the modern morphological disparity.

This approach serves as a powerful, scalable new method for macroevolution. By synthesising computer vision with evolutionary biology, this “pan-phenomic” framework offers a novel perspective on the drivers of biodiversity, enabling the analysis of morphological evolution at a scale previously unattainable.

Code and data accessibility

- Code for data processing: <https://github.com/sun-jiao/osea>
- Code for model training: <https://github.com/sun-jiao/MetaFGNet>
- Code for biological analysis: https://github.com/sun-jiao/osea_morpho_evo
- Model weights: <https://huggingface.co/sunjiao/osea>

Conflict of interests The author has no conflict of interests.

Author contribution statements JS designed the project, programmed the python script and drafted the manuscript.

References

Ansel, J., Yang, E., He, H., Gimelshein, N., Jain, A., Voznesensky, M., Bao, B., Bell, P., Berard, D., Burovski, E., Chauhan, G., Chourdia, A., Constable, W., Desmaison, A., DeVito, Z., Ellison, E., Feng, W., Gong, J., Gschwind, M., et al. (2024). Pytorch 2: Faster machine learning through dynamic python bytecode transformation and graph compilation. *Proceedings of the 29th ACM International Conference on Architectural Support for Programming Languages and Operating Systems, Volume 2*, 929–947. <https://doi.org/10.1145/3620665.3640366>

Cody, M. L. (1973). Coexistence, coevolution and convergent evolution in seabird communities. *Ecology*, 54(1), 31–44. <https://doi.org/10.2307/1934372>

Farid, H. (2021). An overview of perceptual hashing. *Journal of Online Trust and Safety*, 1(1). <https://doi.org/10.54501/jots.v1i1.24>

Felsenstein, J. (1985). Phylogenies and the comparative method. *The American Naturalist*, 125(1), 1–15. <https://doi.org/10.1086/284325>

Fidler, A. E., Kuhn, S., & Gwinner, E. (2004). Convergent evolution of strigiform and caprimulgiform dark-activity is supported by phylogenetic analysis using the arylalkylamine N-acetyltransferase (aanat) gene. *Molecular Phylogenetics and Evolution*, 33(3), 908–921. <https://doi.org/10.1016/j.ympev.2004.08.015>

Geirhos, R., Rubisch, P., Michaelis, C., Bethge, M., Wichmann, F. A., & Brendel, W. (2019). ImageNet-trained CNNs are biased towards texture; increasing shape bias improves accuracy and robustness. *International Conference on Learning Representations*. <https://doi.org/10.48550/arXiv.1811.12231>

Gill, F., Donsker, D., & Rasmussen, P. (2021). IOC world bird list 10.1. <https://doi.org/10.14344/IOC.ML.10.1>

Gill, F., Donsker, D., & Rasmussen, P. (2025). IOC world bird list 15.1. <https://www.worldbirdnames.org/new/ioc-lists/master-list-2/>

Glenny, F. H. (1946). A systematic study of the main arteries in the region of the heart – Aves XI: Tinamiformes – with some notes on their apparent relationship with the Galliformes. *Canadian Journal of Research*, 24(2), 31–38. <https://doi.org/10.1139/cjr46d-004>

Gommers, R., Virtanen, P., Haberland, M., Burovski, E., Reddy, T., Weckesser, W., Oliphant, T. E., Cournapeau, D., Nelson, A., alexbrc, Roy, P., Peterson, P., Polat, I., Wilson, J., endolith, Mayorov, N., van der Walt, S., Colley, L., Brett, M., et al. (2025). *Scipy/scipy: Scipy 1.15.0*. Zenodo. <https://doi.org/10.5281/zenodo.14593523>

Guillerme, T., Cooper, N., Brusatte, S. L., Davis, K. E., Jackson, A. L., Gerber, S., Goswami, A., Healy, K., Hopkins, M. J., Jones, M. E. H., Lloyd, G. T., O'Reilly, J. E., Pate, A., Puttick, M. N., Rayfield, E. J., Saupe, E. E., Sherratt, E., Slater, G. J., Weisbecker, V., et al. (2020). Disparities in the analysis of morphological disparity. *Biology Letters*, 16(7), 20200199. <https://doi.org/10.1098/rsbl.2020.0199>

Haffer, J. (1977). A systematic review of the neotropical ground cuckoos (Aves, Neomorphus). *Bonner zoologische Beiträge : Herausgeber: Zoologisches Forschungsinstitut und Museum Alexander Koenig, Bonn*, 28, 48–76. <https://www.biodiversitylibrary.org/part/119218>

He, K., Zhang, X., Ren, S., & Sun, J. (2016). Deep residual learning for image recognition. *2016 IEEE Conference on Computer Vision and Pattern Recognition (CVPR)*, 770–778. <https://doi.org/10.1109/CVPR.2016.90>

Hedges, S. B., & Sibley, C. G. (1994). Molecules vs. morphology in avian evolution: The case of the "pelecaniform" birds. *Proceedings of the National Academy of Sciences*, 91(21), 9861–9865. <https://doi.org/10.1073/pnas.91.21.9861>

Huerta-Cepas, J., Serra, F., & Bork, P. (2016). Ete 3: Reconstruction, analysis, and visualization of phylogenomic data. *Molecular Biology and Evolution*, 33(6), 1635–1638. <https://doi.org/10.1093/molbev/msw046>

Jónsson, K. A., Fabre, P.-H., Fritz, S. A., Etienne, R. S., Ricklefs, R. E., Jørgensen, T. B., Fjeldså, J., Rahbek, C., Ericson, P. G., Woog, F., et al. (2012). Ecological and evolutionary determinants for the adaptive radiation of the madagascar vangas. *Proceedings of the National Academy of Sciences*, 109(17), 6620–6625. <https://doi.org/10.1073/pnas.1115835109>

LeCun, Y., Boser, B., Denker, J. S., Henderson, D., Howard, R. E., Hubbard, W., & Jackel, L. D. (1989). Backpropagation applied to handwritten zip code recognition. *Neural Computation*, 1(4), 541–551. <https://doi.org/10.1162/neco.1989.1.4.541>

Mei, J., & Dong, H. (2020). *The DongNiao international birds 10000 dataset* (2). arXiv: 2010.06454. <https://doi.org/10.48550/arXiv.2010.06454>

Norberg, U. M. (1986). Evolutionary convergence in foraging niche and flight morphology in insectivorous aerial-hawking birds and bats. *Ornis Scandinavica (Scandinavian Journal of Ornithology)*, 17(3), 253–260. <https://doi.org/10.2307/3676835>

Reddy, S., Driskell, A., Rabosky, D., Hackett, S. J., & Schulenberg, T. (2012). Diversification and the adaptive radiation of the vangas of madagascar. *Proceedings of the Royal Society B: Biological Sciences*, 279(1735), 2062–2071. <https://doi.org/10.1098/rspb.2011.2380>

Ren, S., He, K., Girshick, R., & Sun, J. (2017). Faster R-CNN: Towards real-time object detection with region proposal networks. *IEEE Transactions on Pattern Analysis and Machine Intelligence*, 39(6), 1137–1149. <https://doi.org/10.1109/TPAMI.2016.2577031>

Rotthowe, K., & Starck, J. (1998). Evidence for a phylogenetic position of button quails (Turnicidae: Aves) among the Gruiformes. *Journal of Zoological Systematics and Evolutionary Research*, 36(1-2), 39–51. <https://doi.org/10.1111/j.1439-0469.1998.tb00776.x>

Selvaraju, R. R., Cogswell, M., Abhishek, D., Ramakrishna, V., Devi, P., & Dhruv, B. (2020). Grad-CAM: Visual explanations from deep networks via gradient-based localization. *International Journal of Computer Vision*, 128(2), 336–359. <https://doi.org/10.1007/s11263-019-01228-7>

Simpson, G. G. (1944). *Tempo and mode in evolution*. Columbia University Press.

Stiller, J., Feng, S., Chowdhury, A.-A., Rivas-González, I., Duchêne, D. A., Fang, Q., Deng, Y., Kozlov, A., Stamatakis, A., Claramunt, S., et al. (2024). Complexity of avian evolution revealed by family-level genomes. *Nature*, 629(8013), 851–860. <https://doi.org/10.1038/s41586-024-07323-1>

Wang, F., Xiang, X., Cheng, J., & Yuille, A. L. (2017). NormFace: L_2 hypersphere embedding for face verification. *Proceedings of the 25th ACM International Conference on Multimedia*, 1041–1049. <https://doi.org/10.1145/3123266.3123359>

Williams, C. L., Hagelin, J. C., & Kooymann, G. L. (2015). Hidden keys to survival: The type, density, pattern and functional role of emperor penguin body feathers. *Proceedings of the Royal Society B: Biological Sciences*, 282(1817), 20152033.

Winkler, D. W., Billerman, S. M., & Lovette, I. J. (2020a). Cotingas (Cotingidae). In S. M. Billerman, B. K. Keeney, P. G. Rodewald, & T. S. Schulenberg (Eds.), *Birds of the world*. Cornell Lab of Ornithology. <https://doi.org/10.2173/bow.coting1.01>

Winkler, D. W., Billerman, S. M., & Lovette, I. J. (2020b). Lyrebirds (Menuridae). In S. M. Billerman, B. K. Keeney, P. G. Rodewald, & T. S. Schulenberg (Eds.), *Birds of the world*. Cornell Lab of Ornithology. <https://doi.org/10.2173/bow.menuri1.01>

Wu, Y., Yan, Y., Zhao, Y., Gu, L., Wang, S., & Johnson, D. H. (2021). Genomic bases underlying the adaptive radiation of core landbirds. *BMC Ecology and Evolution*, 21(1), 162. <https://doi.org/10.1186/s12862-021-01888-5>

Zhang, Y., Tang, H., & Jia, K. (2018). Fine-grained visual categorization using meta-learning optimization with sample selection of auxiliary data. *European Conference on Computer Vision*, 241–256. https://doi.org/10.1007/978-3-030-01237-3_15